



**HAL**  
open science

## Synergistic effect of plasma and laser processes in liquid for alloyed nanoparticles synthesis

Natalie Tarasenko, Alexandre Nominé, Alena Nevar, Mikhail Nedelko, Hiba Kabbara, Stéphanie Bruyere, Jaafar Ghanbaja, Cédric Noël, Andrei Krasilin, George Zograf, et al.

### ► To cite this version:

Natalie Tarasenko, Alexandre Nominé, Alena Nevar, Mikhail Nedelko, Hiba Kabbara, et al.. Synergistic effect of plasma and laser processes in liquid for alloyed nanoparticles synthesis. *Physical Review Applied*, 2020, 13 (1), 10.1103/PhysRevApplied.13.014021 . hal-02549011

**HAL Id: hal-02549011**

**<https://hal.science/hal-02549011>**

Submitted on 21 Apr 2020

**HAL** is a multi-disciplinary open access archive for the deposit and dissemination of scientific research documents, whether they are published or not. The documents may come from teaching and research institutions in France or abroad, or from public or private research centers.

L'archive ouverte pluridisciplinaire **HAL**, est destinée au dépôt et à la diffusion de documents scientifiques de niveau recherche, publiés ou non, émanant des établissements d'enseignement et de recherche français ou étrangers, des laboratoires publics ou privés.

# Take the most of both: Synergistic effect of plasma and laser processes in liquid for alloyed nanoparticles synthesis

Natalie Tarasenko,<sup>1,\*</sup> Alexandre Nominé,<sup>2</sup> Alena Nevar,<sup>1</sup> Mikhail Nedelko,<sup>1</sup> Hiba Kabbara,<sup>3</sup> Stéphanie Bruyère,<sup>3</sup> Jaafar Ghanbaja,<sup>3</sup> Cédric Noel,<sup>3</sup> Andrei Krasilin,<sup>2,4</sup> George Zograf,<sup>2</sup> Valentin Milichko,<sup>2</sup> Nikita Kulachenkov,<sup>2</sup> Sergey Makarov,<sup>2</sup> Thierry Belmonte,<sup>3</sup> and Nikolai Tarasenko<sup>1</sup>

<sup>1</sup>*B.I. Stepanov Institute of Physics, National Academy of Sciences of Belarus*

<sup>2</sup>*ITMO University, St. Petersburg 197101, Russia*

<sup>3</sup>*Institut Jean Lamour - CNRS - Université de Lorraine - Nancy, France*

<sup>4</sup>*Ioffe Institute, St. Petersburg, Russia*

Cu-Ag alloy nanoparticles (NPs) have been synthesized from micropowders of pure Cu and Ag using consecutively two non-equilibrium processes based on plasma and lasers in liquids. Plasma process reduces the size of initial micrometric powders down to nanometric size at which the laser fluence is sufficient to melt them, making alloying possible. Measurements at macroscopic (solution absorption), microscopic (scattering of individual NPs) and nanoscopic (electron microscopy) scales confirm alloying of NPs and homogenization in size and composition. This has noticeable effect on the final colloidal solution that absorbs yellow-orange light (550 - 600 nm) after laser treatment. The possibility to quench the as-formed liquid alloy leads to phase compositions that are not compliant with the phase diagram. With a synthesis rate of 360 mg/h, this process opens up interesting perspectives for non-equilibrium nanometallurgy of functional NPs.

## 1. INTRODUCTION

Production of nanoparticles (NPs) represents nowadays a large market with applications in various fields such as catalysis [1], solar cells [2], energy storage [3, 4] bio-imaging [5, 6], drug delivery [7, 8], nanophotonics [9], etc. These fields are directly connected to societal challenges such as global warming, sustainable use of resources or cancer treatment. Therefore, the level of device performance associated with these challenges necessitates to go beyond the conventional approaches and conventional materials [10, 11].

One direction consists in tailoring NPs by their shape [12, 13], another approach consists in tuning their composition [14], the combination of both is also actively investigated [15–17]. In addition to these features, arises the question of the process that would ideally combine the following merits: being upscalable, fast, environmental-friendly, efficient and inexpensive.

Non-equilibrium processes (laser-induced [18], plasma-enhanced [19], microwave-assisted [20], carbothermal [14] etc.) attract an increasing attention for the synthesis of complex nanomaterials (alloys, core-shell, multimetallic) as they involve both locally and temporally extreme conditions of temperature and pressure (and their gradients) that could not be attained otherwise [21]. If very locally temperature reaches several thousand degrees and pressure several hundred bars, all these processes are macroscopically run at room temperature and atmospheric pressure, which represents a strong asset for industrial development.

Electrical discharges submerged in liquids are known as ultra-fast processes to synthesize NPs from bulky elec-

trodes. They present the main advantage of being inexpensive, safe and easy to run. They have been successfully used to synthesize core-shell NPs [22, 23], nano-sheets [22], and even to discover new crystallographic phases [24]. However, these processes do not provide sufficiently-narrowed size distributions yet.

Laser synthesis and processing for nanomaterials synthesis has been extensively studied over the last decade [25]. The most widespread process is probably the laser ablation in liquids (LAL) that consists in ablating a bulk target [26–28]. Another approach, known as laser melting in liquids (LML) [29, 30], consists in irradiating a colloidal solution by a laser beam. This leads to local melting of NPs with the possibility of adjusting their size at the sub-micrometer or nanometer scale [31]. LML has also been successfully used to alloy NPs, mixing two colloidal solutions of pure compounds and irradiating the mixture by a nanosecond-pulsed laser [32].

In the present study, we investigate the interest of combining a plasma process - efficient to reduce the mean size distribution of microscopic particles down to the nanoscale - and a laser post-treatment of the plasma-treated colloidal solution - expected to promote alloying of particles. Here, we limit our study to the Cu-Ag system for several reasons. Firstly, the phase diagram is simple, with a limited concentration of either element into the other, the absence of defined compound and a single eutectic [33]. Secondly, this system is considered as a potential low-cost alternative to Au and Pt in catalysis [34] or photonics [35]. Thirdly, Cu-Ag system could be used in a large range of applications such as medicine [35], sensors [36], microelectronics [37], and has even been found in archaeological remains [38, 39].

The present study focuses on the optical properties of single Cu-Ag NPs and their colloidal solutions, with the objective of bridging synthesis process, NPs characteri-

---

\* [nat.tarasenko@gmail.com](mailto:nat.tarasenko@gmail.com)

zation and optical properties.

## 2. MATERIALS AND METHODS

### 2.1. Synthesis

NPs were prepared by a two-step process composed of an electrical discharge (ED) treatment of a mixture of Ag and Cu micro-powders dispersed in ethanol followed by laser irradiation of the formed colloid. First, a 1:1 mixture of Ag and Cu micro-powders was dispersed in ethanol and processed in the suspension by submerged electrical discharges. For the synthesis of alloyed NPs from a mixture of precursors (powders with micrometre size), a reactor cell with a special discharge configuration was constructed.

The discharge was ignited in the fluoroplastic funnel-shaped cell between two coaxial vertically-orientated tungsten electrodes (Fig. 1a). A conical shape of the cell prevented removal of particles from the discharge area providing plasma processing of particles during a suited time interval. The optimal distance between the electrodes was kept constant at approximately 2 mm to maintain a stable discharge. The discharge was initiated by applying a high-frequency voltage of 8.5 kV. The power supply provided an alternating current (ac) that fed a spark discharge at a repetition rate of 100 Hz. The electric circuit with a relaxation time pulse generator provided a typical oscillating discharge current with high peak (10-12A) intensity and a duration of a single discharge pulse of 2-5  $\mu$ s. Oscillations were damped quickly with a decay time of 40-50  $\mu$ s. The overall duration of the plasma treatment process was 5 min.

After the discharge treatment, prepared colloids were exposed to a laser irradiation. For this purpose, 2 ml of the colloid was diluted with ethanol in 1:1 ratio and subjected to 532 nm laser irradiation with unfocused beam of the second harmonics of the Nd:YAG laser (LOTIS, wavelength 532 nm, frequency 10 Hz, pulse duration 10 ns, pulse energy 60 and 100 mJ/pulse, exposure time 5 min). Due to residual micro-particles that have been filtered before further analysis, it remains difficult to accurately determine the NPs production rate. However, we estimated this amount to be around 360 mg/h. The estimation of the elements concentration in the prepared colloid was performed by inductively coupled plasma optical emission spectroscopy calibrated by standard water solutions.

### 2.2. Plasma Diagnostics

Spectroscopic studies of plasmas were performed using a diffraction spectrometer equipped with a CCD linear array. The light emitted by the plasma was focused by lenses with a focal length of 15 cm on the entrance slit of the spectrometer with a 1200 gr/mm grating in order to

investigate the spectral region from 300 nm to 700 nm. The operation of the detection system was controlled by a computer via a USB interface, using the CCD software tool. The identification procedure took into account the spectral positions of the lines and their intensities (height of the line minus the background) in comparison with the relative intensities (or transition probabilities) provided by the National Institute of Standards and Technology (NIST) database.

### 2.3. Characterization

Transmission electron microscopy (TEM) investigations were carried out using a JEM - ARM 200F Cold FEG TEM/STEM operating at 200 kV and equipped with a spherical aberration (Cs) probe and image correctors (point resolution: 0.12 nm in TEM mode and 0.078 nm in STEM mode).

UV-Vis absorption spectra of colloidal solutions were recorded immediately after preparation in a 0.5 cm quartz cuvette using the Cary 500 spectrometer. Plasmon resonance of individual NPs was determined by white light scattering in the dark field geometry. For this, a droplet of solution was deposited onto a fused silica substrate. The subsequent solvent evaporation leaves NPs on the substrate with a low surface density (0.1 particle per square micrometer typically). A home-made dark-field scheme was used [40] where the NPs were illuminated by s-polarized light from a halogen lamp (HL-2000-FHSA) at an angle of 65° with respect to the substrate normal. The scattered signal was collected by an objective (Mitutoyo M Plan APO NIR 50, NA = 0.45) and then analyzed by a commercial confocal spectrometer (Horiba LabRam HR with a cooled CCD camera, Andor DU 420A-OE 325, and 600 g/mm diffraction grating).

## 3. RESULTS

### 3.1. Optical properties of NPs

The effect of combined plasma-laser treatment is visible to the naked eye (Fig. 2a). Firstly, the residue settled down to the bottom of the vessel after plasma treatment disappears during laser treatment. Secondly, the colloidal solution turns from a slightly turbid and colorless aspect to a well-defined orange color. This is associated with a decrease in absorption over the whole visible spectrum (Fig. 2b) and also with the appearance of an absorption hump at yellow-orange wavelengths (550-600 nm).

Observation of NPs in Dark-Field configuration (Fig. 2b) reveals the presence of a large amount of nano-scatterers, equally before and after laser treatment. However, after plasma treatment only, the scattering - attributed to Localized Surface Plasmon Resonance (LSPR) - is observed in the range 670-730 nm while after

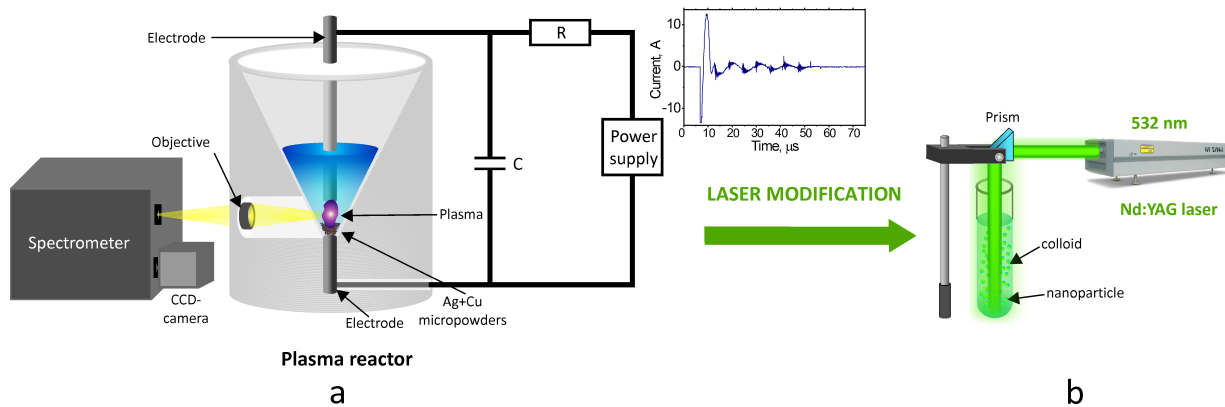


Figure 1. **Scheme of the two-step process with a 5 min plasma treatment (a) followed by a 5 min laser treatment (b)**

laser treatment, LSPR is blue-shifted to the range 560-640 nm (Fig. 2d). A narrowing of the LSPR profile is also associated with laser post-treatment.

### 3.2. Characterization of NPs

Fig. 3 shows that the plasma treatment significantly reduces the average size of pristine particles. Indeed, from an initial average diameter of 1  $\mu\text{m}$ , particles are reduced down to the nanometre range. In Figs. 3b and 3e, one can notice that the size reduction is more efficient for Ag-rich particles that lie within the radius range [10-60 nm] than for Cu particles that lie within the radius range [15-275 nm]. This effect is erased by the subsequent laser post-treatment that homogenizes the NPs, regardless their composition, towards radius range [10-65 nm].

Alloyed NPs are already observed after the sole plasma treatment unlike what had been reported for a pin-to-pin configuration, with electrodes made of pure Cu and Ag [41]. This shows some difference in the physical processes at stake when using powders rather than bulk electrode as the initial source material. However and, as suggested above, the distribution in composition is particularly broad (Fig. 3e). A significant proportion of NPs remains unalloyed and coexist with alloyed NPs covering the full composition range. After laser treatment the composition distribution is narrowed towards the composition range [37-70 Cu at%].

### 3.3. Plasma Diagnostics

The typical OES spectra of the plasma formed during electrical discharge processing of Ag and Cu powders mixture are presented in Fig. 4a. These results reveal the presence of spectral lines of Cu and Ag atoms (Cu I 510.55 nm, Cu I 521.77 nm, Ag I 520.82 nm, Ag I 546.30 nm) as well as ions (Cu II 505.30 nm, Ag II 539.98 nm) along with  $H\alpha$ ,  $H\beta$  lines (Fig. 4a,b) and  $C_2$  Swan

band (Fig. 4a,c). The presence of metallic excitation lines comes from micro/nano powders while the Hydrogen lines and the  $C_2$  band that can be related to ethanol decomposition. The analysis of the  $H\alpha$  line broadening (Fig. 4b) allows the determination of the plasma electron density  $n_e$  using the relation for Stark broadening:

$$\Delta\lambda = 2.5 \cdot 10^9 \cdot \alpha_{H\alpha} \cdot n_e^{2/3} \quad (1)$$

where  $\alpha_{H\alpha}$  is the broadening parameter,  $\Delta\lambda$  the FWHM of the  $H\alpha$  line calculated from a Lorentzian fit. The measured value of the broadening  $\Delta\lambda$  was 1.86 nm and the calculated value of the electron density was found to be  $3.3 \cdot 10^{17} \text{ cm}^{-3}$ .

## 4. DISCUSSION

### 4.1. Formation of NPs

#### 4.1.1. Plasma Process

Determination of plasma temperature, especially with the aim of specifying synthesis conditions of materials, necessitates to take several precautions [42, 43]. A common pitfall is to consider the electron temperature  $T_e$  equal to the gas temperature  $T_{gas}$  and integrate it directly in further thermal transfer calculation. Actually, transition levels of excitation processes are in the range of several eV (*i.e.* several  $10^4$  K), those of vibrational levels in the range of a few tenths of eV (*i.e.* several  $10^3$  K) and those of rotational levels in the range of a few hundredths of eV (*i.e.* several 100s K). Therefore, the following ranking can be established:

$$T_{ex} \approx T_e \geq T_{vib} \geq T_{rot} \approx T_{gas} \quad (2)$$

The only case when  $T_e$  may be directly considered as the process temperature is when the discharge is at ther-

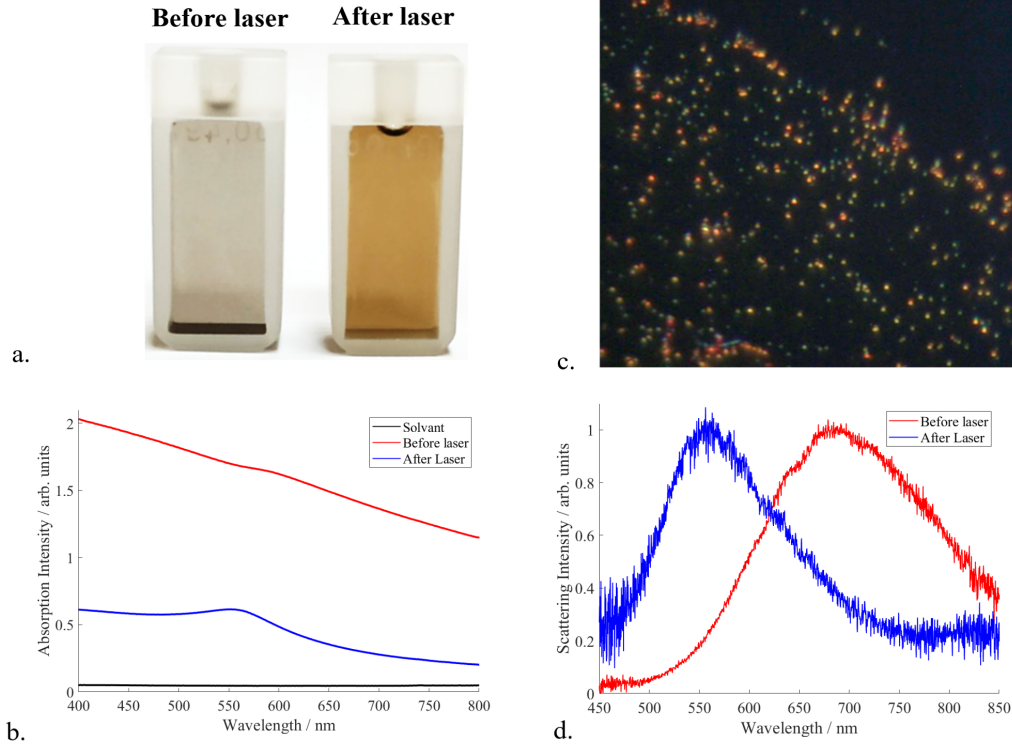


Figure 2. Image of colloidal solutions before and after laser treatment (a), and associated absorption spectra (b). Micrograph in Dark-field configuration of the sample after laser irradiation revealing the presence of nano-scatterers (c) and their associated scattering spectra (d)

modynamic equilibrium. Since it is the exception rather than the rule in low-temperature plasmas, it is always preferable to use rotational temperature to estimate the gas temperature when possible. Here, gas temperature has been determined thanks to the rotational temperature of the  $C_2$  Swan band (Fig. 4c). For a diatomic molecule, the emission intensity is given by (3) where  $S$  is the oscillator strength of the transition and  $E$  is the energy of the upper level.  $n$ ,  $v$  and  $J$  refer respectively to electronic, vibrational and rotational excitation levels from upper and lower states of the transition. A least squares method is used to get the best agreement between an experimental spectrum and a calculated one with  $T_{rot}$  as an optimization variable.

$$I(\lambda) \propto S(n', v', J', n'', v'', J'') \cdot \exp\left(-\frac{E_{n'', v'', J''}}{k \times T_{rot}}\right) \quad (3)$$

In the present case, the best fitting result was found for a rotational temperature of  $4,400 \pm 100$  K. This is several times above the melting temperatures and even the vaporization points of silver and copper [44]. Despite these presumably favorable conditions, the alloying efficiency of the plasma process is poor, as discussed previously (Fig. 3b). This can be attributed to two main reasons:

- the small discharge volume, about  $10^{-5} \text{ mm}^3$  only.

The volume that is brought at high temperature is only a small fraction of the total reactor volume.

- the high pressure reached during breakdown generates an "explosion-like" force field that pushes NPs far from each other [45]

If these conditions are not optimal for alloying, they are perfectly suited to reducing the size of microparticles.

#### 4.1.2. Laser post-treatment

The models of laser interaction with colloidal nanoparticles are based on the balance between laser energy absorbed by the NP and the dissipation due to heat losses [46–49]. This concept can be mathematically formalized as follows:

$$E_{abs} = E_{th}^{melt} + E_{melt} + E_{th}^{boil} \quad (4)$$

where  $E_{abs}$  represents the energy absorbed by the NP,  $E_{th}^{melt}$  - the thermal energy necessary to reach the melting point  $T_m$ ,  $E_{melt}$  - the melting energy, and  $E_{th}^{boil}$  the thermal energy from the melting point to the boiling point  $T_b$ . These quantities are respectively estimated by the

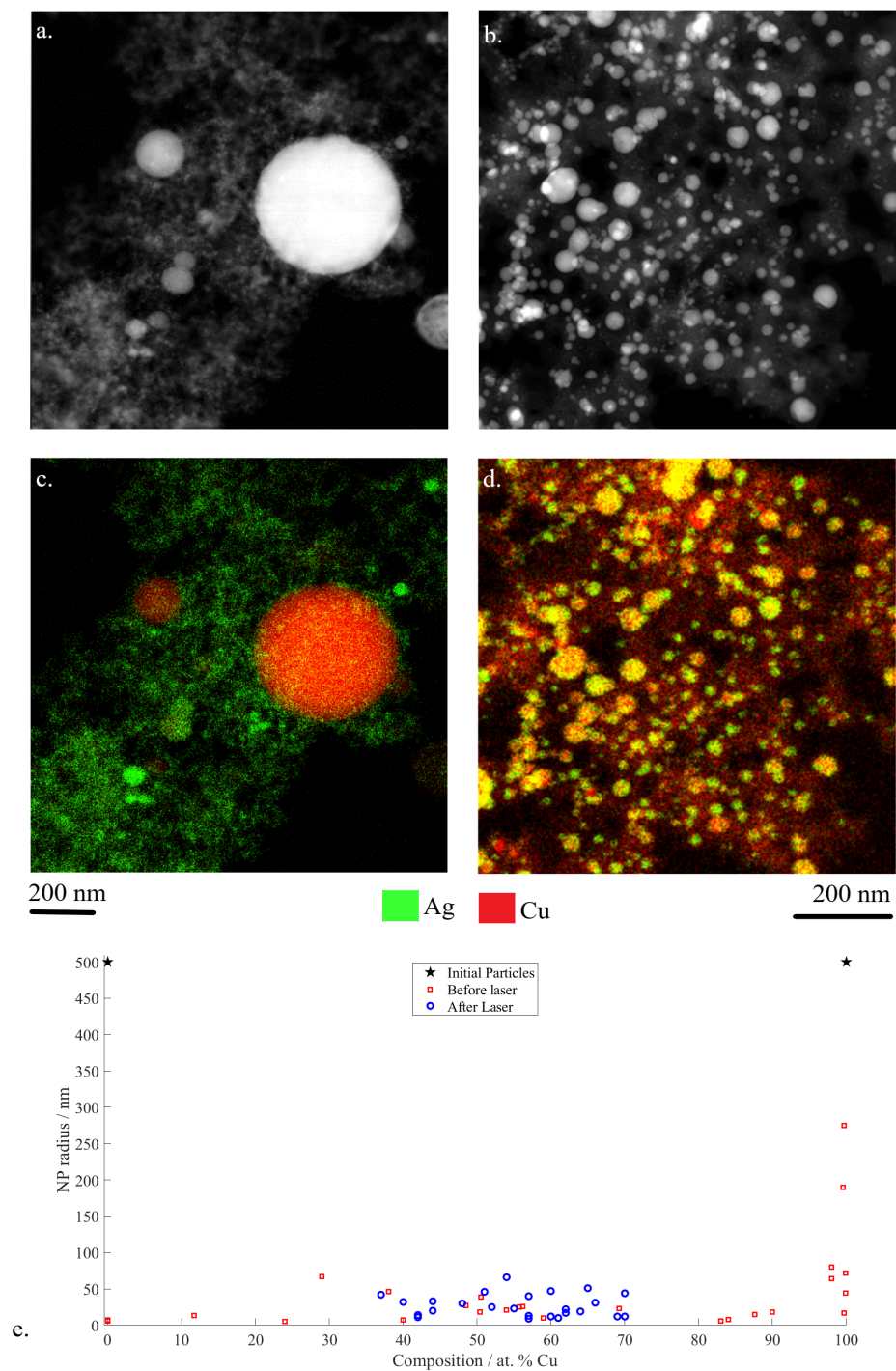


Figure 3. Scanning Transmission Electron Microscopy High-angle annular dark-field (STEM-HAADF) micrographs (a,c) and EDS mapping (b,d) of Cu-Ag NPs synthesized by plasma treatment (a,b) and combined plasma-laser treatment (c,d). NPs size-composition distribution (e)

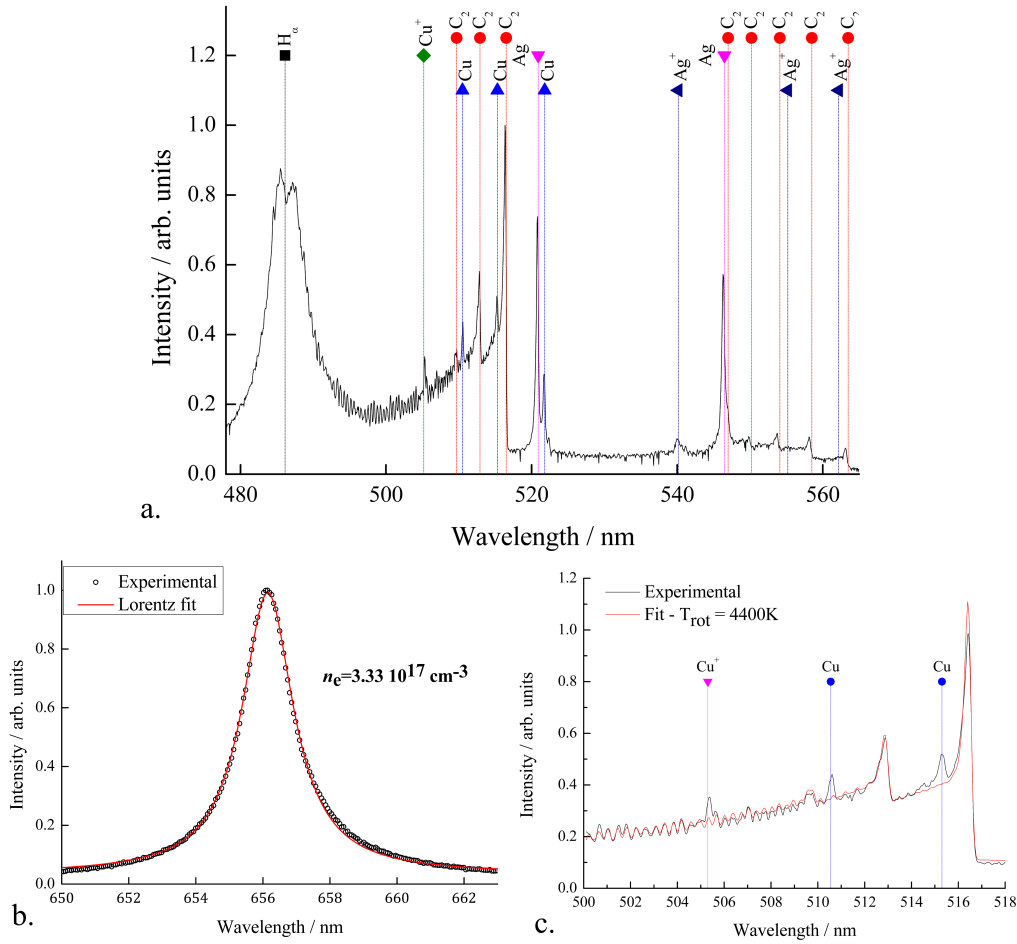


Figure 4. **Optical emission spectra showing the presence of both metallic elements as well as C $_2$  and H lines (a) H $\alpha$  line profile used to determine the electron density (b) and molecular C $_2$  Swan system used to determine the rotational temperature (c)**

following equations:

$$E_{abs} = \sigma_{abs}^{\lambda} \cdot \Phi \cdot t_p \quad (5)$$

$\sigma_{abs}^{\lambda}$  being the absorption cross section at a given wavelength,  $\Phi$  the laser irradiance (in  $W \cdot m^{-2}$ ) and  $t_p$  the pulse duration.

$$E_{th}^{melt} = m \cdot C_p^{sol} \cdot \Delta_{T_0}^{T_m} T \quad (6)$$

with  $m$  and  $C_p^{sol}$  the NP mass and heat capacity of the solid, respectively.

$$E_{melt} = m \cdot L_m \quad (7)$$

with  $L_m$  the latent heat of fusion.

$$E_{th}^{boil} = m \cdot C_p^{liq} \cdot \Delta_{T_m}^{T_b} T \quad (8)$$

with  $C_p^{liq}$  the heat capacity of the liquid NP material.

Other possible sources of heat loss, such as radiation or solidification can be neglected in the case of a ns laser

irradiation (see 3.2 in [46]). From the previous equation, we can determine  $\Phi^{melt}$  the threshold irradiance at which NPs suffer a solid - liquid phase transition for a laser wavelength set at 532 nm.  $\Phi^{melt}$  can be expressed as follows:

$$\Phi^{melt} = \frac{E_{th}^{melt} + E_{melt}}{\sigma_{abs}^{532} \cdot t_p} \quad (9)$$

Several quantities depend on the NP radius  $r$ , the composition  $x$  or both. The previous equation is therefore expressed in its expanded form as follows:

$$\Phi^{melt} = \frac{m(r, x) \cdot (C_p^{sol}(x) \cdot (T_m(r, x) - T_0) + L_m(r, x))}{\sigma_{abs}^{532}(r, x) \cdot t_p} \quad (10)$$

The fusion temperature is radius and composition-dependent and is calculated with the equation given by Buffat and Borel [50] :

$$T_m(r, x) = T_m^{bulk}(x) \left( 1 - \frac{2}{r \cdot \rho_s(x) \cdot L_m(x)} \times \left( \sigma_s(x) - \sigma_L(x) \left( \frac{\rho_s(x)}{\rho_L(x)} \right)^{\frac{2}{3}} \right) \right) \quad (11)$$

where  $T_m^{bulk}(x)$  is the melting point of the bulk alloy, taken from the phase diagram,  $\rho_s$  and  $\rho_L$  the density of the solid and liquid alloys respectively,  $\sigma_s$  and  $\sigma_L$  the surface energy of the solid and liquid alloys, respectively.

The cross-section calculation can be determined as follows: [51]:

$$\sigma_{abs}^\lambda(r, x) = \sigma_{ext}^\lambda(r, x) - \sigma_{sca}^\lambda(r, x) \quad (12)$$

$$\sigma_{sca}^\lambda = \frac{2\pi}{k^2} \sum_{n=1}^{\infty} (2n+1) (|a_n|^2 + |b_n|^2) \quad (13)$$

$$\sigma_{ext}^\lambda = \frac{2\pi}{k^2} \sum_{n=1}^{\infty} (2n+1) \text{Re}(a_n + b_n) \quad (14)$$

with  $n$  the multipole order and  $k = \frac{2\pi \cdot n_r}{\lambda}$  with  $n_r$  the real part of the refractive index.  $a_n$  and  $b_n$  the scattering coefficients defined by:

$$a_n = \frac{m\psi_n(mz)\psi'_n(z) - \psi_n(z)\psi'_n(mz)}{m\psi_n(mz)\xi'_n(z) - \xi_n(z)\psi'_n(mz)} \quad (15)$$

$$b_n = \frac{\psi_n(mz)\psi'_n(z) - m\psi_n(z)\psi'_n(mz)}{\psi_n(mz)\xi'_n(z) - m\xi_n(z)\psi'_n(mz)} \quad (16)$$

with  $z = kr$ , and the Riccati-Bessel functions:  $\psi_n(\rho) = \rho j_n(\rho)$ ,  $\xi_n(\rho) = \rho h_n^{(1)}(\rho)$ , where  $j_n$  and  $h_n^{(1)}$  are spherical Bessel and Hankel functions, respectively.

The refractive index of pure copper and silver were taken from Johnson *et. al.* [52]. For the Cu-Ag alloy, data for different compositions (90, 70, 50 and 40 at% Cu) are available in [53]. The evolution of  $\sigma_{abs}^{532}$  is presented in Fig. 5a. The dashed lines represent the contribution of the different multipoles. It is obvious that in the present case (metallic alloys), the contribution of magnetic multipole is negligible compared with the electric multipoles.

$\Phi^{melt}$  has been calculated for the full range of composition and for radius values between 1 nm and 500 nm, *i.e.* up to the initial average size of micropowders (Fig. 5b). In this figure, one can notice that reaching the melting point of pure silver NPs requires an irradiance that is about one order of magnitude higher than for pure Cu NPs of the same size. The experimental irradiance, equal to  $5 \cdot 10^{11} \text{W} \cdot \text{m}^{-2}$  is also plotted in Fig. 5b. It turns out that the irradiance used is sufficient to melt NPs with radii lower than 75 nm, irrespective of their composition. This radius corresponds to the largest Ag NP that can be melted within these conditions of irradiance and pulse

duration. On the other side of the composition range, the critical radius for pure Cu NPs is about 5 times the one of Ag NPs and reaches 390 nm.

The intersection between  $\Phi^{melt}$  and the experimental irradiance is represented by the red dashed line in Fig. 5c. This line separates the radius-composition space into a region where laser melting is possible (below the line) and a region where it is not (above the line). It is interesting to bridge this graph with size and composition distributions at each step of the process. First, one starts with micrometric NPs that cannot be melted and alloyed by laser at this irradiance. The 5 min plasma treatment decreases the size of particles so that the distribution is shifted to regions where laser irradiance is sufficient to melt and alloy NPs. The laser-induced melting results in the alloying of NPs and a homogenization of their size. Note that the plasma treatment reduces more efficiently the size of the NPs that are more difficult to melt by laser, namely the Ag-rich ones. Similarly, the poor efficiency of the plasma treatment in reducing the mean size of Cu particles is compensated by the higher efficiency of laser melting for Cu-rich NPs.

## 4.2. Optical properties of NPs

The challenge to understand the relationship between NPs microstructure and their optical properties relies on the fact that the optical dark-field spectroscopy probes are about  $1 \mu\text{m}^3$  while TEM can reach atomic scale. It is therefore difficult to associate the radius and composition of NPs with their scattering spectra. To overcome this limitation, scattering cross-sections have been calculated (the calculation is detailed in the previous section) in the visible range for seven different compositions of NPs (0, 40, 50, 60, 70, 90, 100 % Cu) and radii (1 to 500 nm). The scattering maps of pure silver, 50% Ag alloy and pure copper are shown in Figs. 6 a-c. It appears that the scattering profiles are red-shifted with an increasing size of NPs or Cu content.

A home-made filtering procedure was developed under a MATLAB environment in order to identify, among the 3500 simulated spectra, the scattering spectra matching experimental data. The input parameters are the number of peaks, their position and their width.

The used parameters are summarized in Table I and were determined from the analysis of several tens of scattering spectra from different NPs. Out of these results, a region of interest (ROI) can be drawn (Fig. 6d). It should be noted at this stage that if the  $(r, x)$  conditions that are not in the ROI can be excluded as candidates for fitting experimental data, it does not guarantee that a  $(r, x)$  couple within the ROI will automatically match

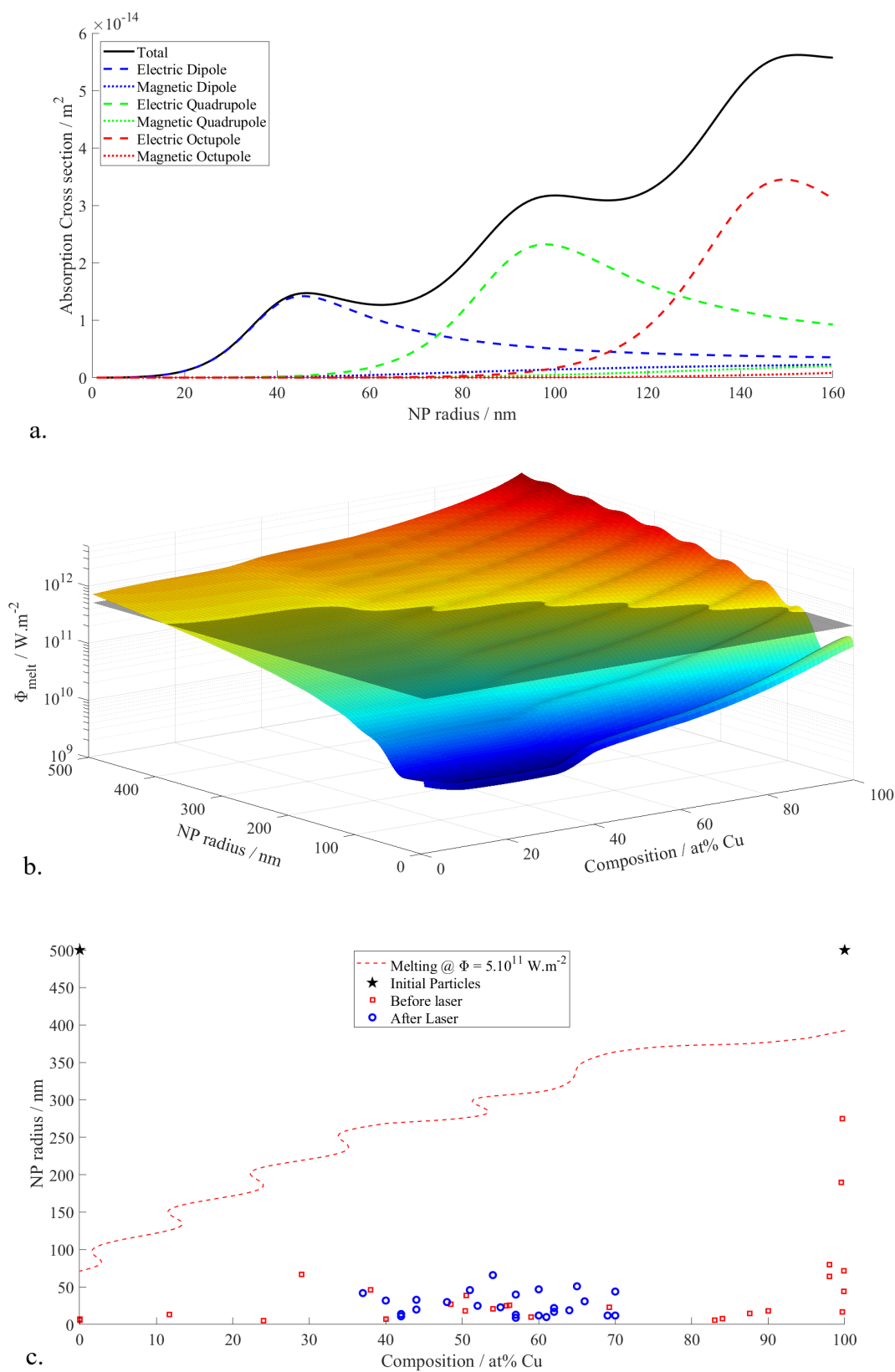


Figure 5. NP radius dependence of absorption cross-section a 50 at % NP composition with the contribution of the different multipoles in dashed lines (a). Melting irradiance as a function of the NP size and composition versus the experimental irradiance, in black, corresponding to  $\Phi = 5 \cdot 10^{11} W \cdot m^{-2}$  (b). In red dashed line, the intersection between the melting irradiance and the experimental irradiance along with the size-composition distributions at each step of the process (c)

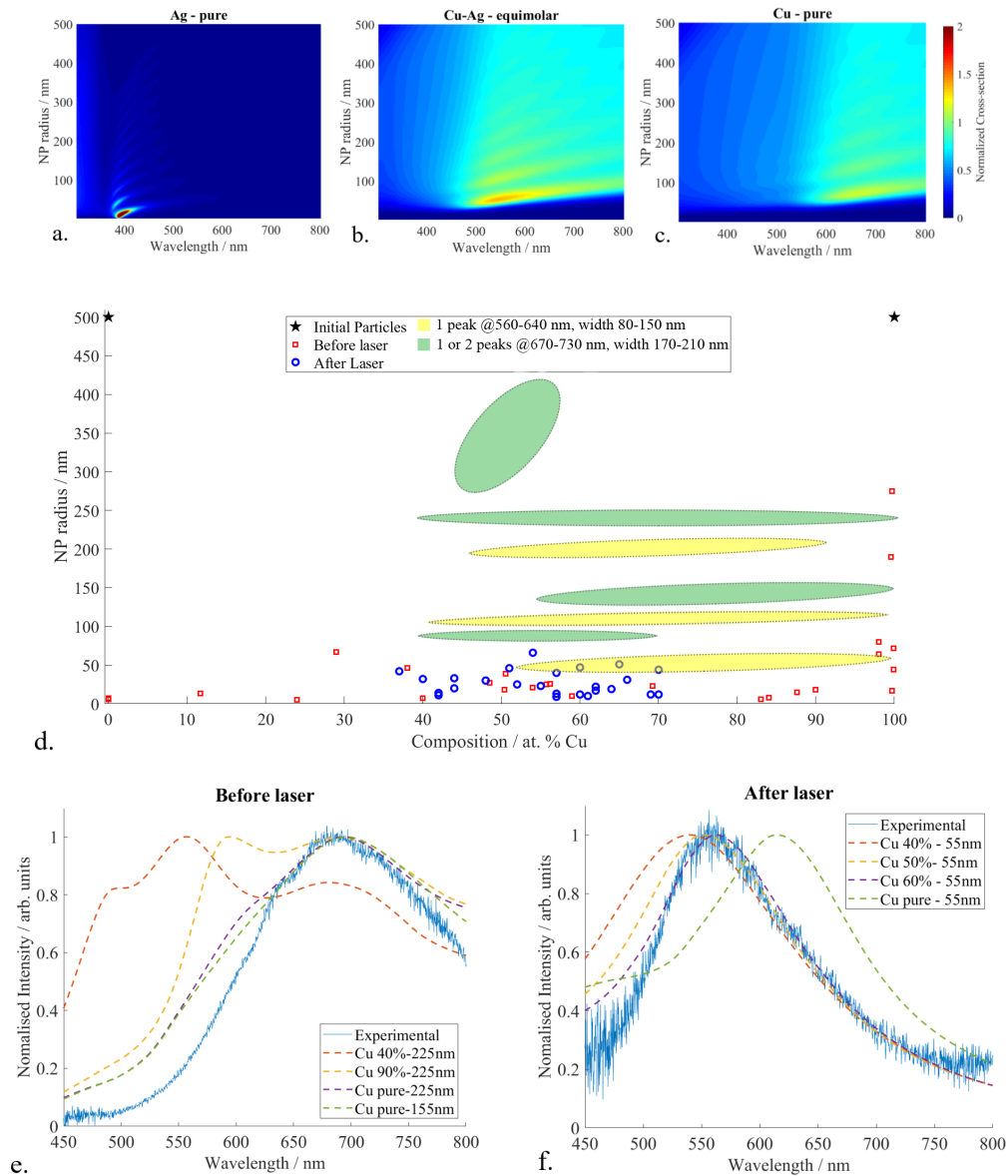


Figure 6. Analytic calculation of the dependence of the scattering cross-section as a function of wavelength and NP radius for different alloy compositions pure Ag (a), 50 % Cu (b), pure Cu (c). Mapping of the region of interest for scattering profile overlapped with NPs size and composition distribution (d). Scattering spectra from Fig. 2d before (e) and after laser treatment (f) with modeled spectra for different NP composition and sizes

experimental data. Overlapping of the ROI with the size and composition distributions from Fig. 6, limits drastically the number of possibilities. The best fit of the typical spectra of a NP synthesized with a single plasma treatment (*i.e.* before laser) is obtained for pure Cu NPs with radius of either 155 or 225 nm. After laser treatment, almost perfect matching is obtained between experimental spectra and modelling results corresponding to a 60% Cu 55nm radius NP.

The fact that the overlap between ROI and NP size and composition distribution is shifted towards higher

Cu concentration might provoke questioning as equal quantities of Cu and Ag are introduced at the beginning of the process. We have to recall that the optical dark-field spectroscopy does not overcome the diffraction limit, which forbids the detection of NPs with radii below 30 nm. From Fig. 3d, we know that such NPs are present but not detected. It is plausible that their detection would have shifted the ROI closer to an equimolar Cu/Ag ratio.

The spectra presented in Fig. 2b have been corrected by the intensity of the spectrum of the solvent in order to

Table I. Parameters for spectra identification.

Parameter	Number of peaks	Peak(s) position (nm)	Peak(s) width (nm)
Before laser	1 or 2	670 - 730	170 - 210
After laser	1	560 - 640	0 - 150

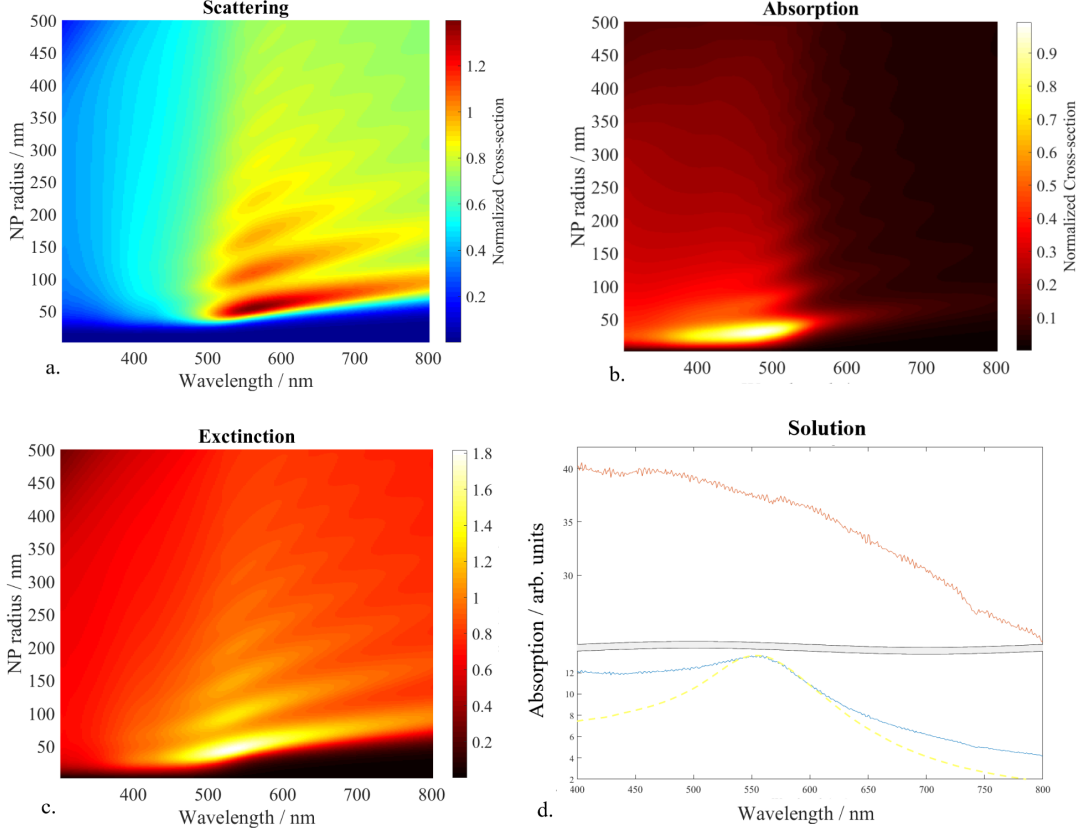


Figure 7. Analytic calculation of the dependence of the scattering (a), absorption (b) and extinction cross-sections (c) for a 60% Cu alloy composition. Absorption spectra from colloidal solution before and after laser treatment and the normalized extinction cross section for a 55 nm NP (d)

obtain the sole contribution of NPs (Fig. 7d). Absorption of the solution is actually composed of both intrinsic absorption of NPs and scattering. Therefore, it is more appropriate to compare the solution absorption with NPs extinction cross-section. The three quantities are represented in Fig. 7 a-c.

Before laser treatment, the absorption spectra do not show any particular features, which is attributed to the large distribution in size and composition. After laser treatment a particular hump appears around 560 nm (Fig. 7d). A satisfying model is obtained by setting the extinction cross-section at that of 55 nm radius and 60% Cu NPs. The acceptable mismatch in the profile before 500 nm and after 650 nm may be attributed to the dispersion in size and composition.

## 5. CONCLUSION

In this paper, we have shown the combination of two non-equilibrium processes based on plasmas and lasers for the synthesis of alloyed NPs. Plasma appears to be efficient to rapidly decrease the mean size distribution of microparticles into sufficiently small NPs to enable their melting by laser irradiation. This latter step contributes to homogenize the NPs in size and composition. Thus-treated NPs are good nano-scatterers in the 560 - 640 nm region. The laser treatment is also useful to transform the turbid and colorless solution, resulting from the plasma treatment into a solution with well defined absorption in the orange region. This combined processing opens up the way to new design of NPs with controlled properties.

## 6. ACKNOWLEDGEMENT

AN is grateful to *ITMO Fellowship* program for financial support. TB, SB and JG benefited from Programme Hubert Curien-Kolmogorov. TB and HK are grateful to Agence Nationale de la Recherche for financial support through CEENEMA project (ANR-15-CE050005).

NT, MN and NT acknowledge financial support from Belarusian Foundation for Fundamental Researches under Grant No. F 18MS-005. SM acknowledges the Ministry of Education and Science of the Russian Federation (Project 16.8939.2017/8.9).

- 
- [1] G. Prieto, J. Zeevi, H. Friedrich, K. P. de Jong, and P. E. de Jongh, *Nature Materials* **12**, 34 (2013).
- [2] W. J. E. Beek, M. M. Wienk, and R. a. J. Janssen, *Advanced Materials* **16**, 1009 (2004).
- [3] S. Choudhury, R. Mangal, A. Agrawal, and L. A. Archer, *Nature Communications* **6**, 10101 (2015).
- [4] Y. Jiao, D. Han, Y. Ding, X. Zhang, G. Guo, J. Hu, D. Yang, and A. Dong, *Nature Communications* **6**, 6420 (2015).
- [5] N. A. Frey, S. Peng, K. Cheng, and S. Sun, *Chemical Society Reviews* **38**, 2532 (2009).
- [6] M. V. Zyuzin, D. G. Baranov, A. Escudero, I. Chakraborty, A. Tsympkin, E. V. Ushakova, F. Kraus, W. J. Parak, and S. V. Makarov, *Scientific Reports* **8**, 6107 (2018).
- [7] M. V. Yezhelyev, X. Gao, Y. Xing, A. Al-Hajj, S. Nie, and R. M. O'Regan, *The Lancet Oncology* **7**, 657 (2006).
- [8] A. S. Timin, A. R. Muslimov, M. V. Zyuzin, O. O. Pelttek, T. E. Karpov, I. S. Sergeev, A. I. Dotsenko, A. A. Goncharenko, N. D. Yolshin, A. Sinelnik, B. Krause, T. Baumbach, M. A. Surmeneva, R. V. Chernozem, G. B. Sukhorukov, and R. A. Surmenev, *ACS Applied Materials & Interfaces* **10**, 34849 (2018).
- [9] J.-H. Park, C. Park, H. Yu, J. Park, S. Han, J. Shin, S. H. Ko, K. T. Nam, Y.-H. Cho, and Y. Park, *Nature Photonics* **7**, 454 (2013).
- [10] G. V. Naik, V. M. Shalaev, and A. Boltasseva, *Advanced Materials* **25**, 3264 (2013).
- [11] K. Domanski, J.-P. Correa-Baena, N. Mine, M. K. Nazeeruddin, A. Abate, M. Saliba, W. Tress, A. Hagfeldt, and M. Graetzel, *ACS Nano* **10**, 6306 (2016).
- [12] M. Grzelczak, J. Prez-Juste, P. Mulvaney, and L. M. Liz-Marzn, *Chemical Society Reviews* **37**, 1783 (2008).
- [13] S. Chen, Z. L. Wang, J. Ballato, S. H. Foulger, and D. L. Carroll, *Journal of the American Chemical Society* **125**, 16186 (2003).
- [14] Y. Yao, Z. Huang, P. Xie, S. D. Lacey, R. J. Jacob, H. Xie, F. Chen, A. Nie, T. Pu, M. Rehwoldt, D. Yu, M. R. Zachariah, C. Wang, R. Shahbazian-Yassar, J. Li, and L. Hu, *Science* **359**, 1489 (2018).
- [15] Z. Peng and H. Yang, *Nano Today* **4**, 143 (2009).
- [16] R. He, Y.-C. Wang, X. Wang, Z. Wang, G. Liu, W. Zhou, L. Wen, Q. Li, X. Wang, X. Chen, J. Zeng, and J. G. Hou, *Nature Communications* **5**, 4327 (2014).
- [17] N. TienKhi, H. Baik, H. Lee, J. Yoon, J.-H. Sohn, and K. Lee, *Nanoscale* **6**, 11007 (2014).
- [18] S. V. Makarov, M. I. Petrov, U. Zywiets, V. Milichko, D. Zuev, N. Lopanitsyna, A. Kuksin, I. Mukhin, G. Zograf, E. Ubyivovk, D. A. Smirnova, S. Starikov, B. N. Chichkov, and Y. S. Kivshar, *Nano Letters* **17**, 3047 (2017).
- [19] K. Ostrikov, E. C. Neyts, and M. Meyyappan, *Advances in Physics* **62**, 113 (2013).
- [20] R. J. Mehta, C. Karthik, W. Jiang, B. Singh, Y. Shi, R. W. Siegel, T. Borca-Tasciuc, and G. Ramanath, *Nano Letters* **10**, 4417 (2010).
- [21] I. Levchenko, K. Bazaka, O. Baranov, R. M. Sankaran, A. Nomine, T. Belmonte, and S. Xu, *Applied Physics Reviews* **5**, 021103 (2018).
- [22] H. Kabbara, J. Ghanbaja, C. Nol, and T. Belmonte, *Nano-Structures & Nano-Objects* **10**, 22 (2017).
- [23] Z. Abdullaeva, E. Omurzak, C. Iwamoto, H. Okudera, M. Koinuma, S. Takebe, S. Sulaimankulova, and T. Mashimo, *RSC Advances* **3**, 513 (2012).
- [24] A. Hamdan, H. Kabbara, C. Nol, J. Ghanbaja, A. Redjaimia, and T. Belmonte, *Particuology* **40**, 152 (2018).
- [25] D. Zhang, B. Gkce, and S. Barcikowski, *Chemical Reviews* **117**, 3990 (2017).
- [26] I. Vassalini, L. Borgese, M. Mariz, S. Polizzi, G. Aquilanti, P. Ghigna, A. Sartorel, V. Amendola, and I. Alessandri, *Angewandte Chemie International Edition* **56**, 6589 (2017).
- [27] V. Amendola, M. Meneghetti, O. M. Bakr, P. Riello, S. Polizzi, D. H. Anjum, S. Fiameni, P. Arosio, T. Orlando, C. d. J. Fernandez, F. Pineider, C. Sangregorio, and A. Lascialfari, *Nanoscale* **5**, 5611 (2013).
- [28] S. Ibrahimkuty, P. Wagener, T. d. S. Rolo, D. Karpov, A. Menzel, T. Baumbach, S. Barcikowski, and A. Plech, *Scientific Reports* **5**, 16313 (2015).
- [29] S. Link, C. Burda, M. B. Mohamed, B. Nikoobakht, and M. A. El-Sayed, *The Journal of Physical Chemistry A* **103**, 1165 (1999).
- [30] J. H. Hodak, A. Henglein, M. Giersig, and G. V. Hartland, *The Journal of Physical Chemistry B* **104**, 11708 (2000).
- [31] H. Wang, A. Pyatenko, K. Kawaguchi, X. Li, Z. Swiatkowska-Warkocka, and N. Koshizaki, *Angewandte Chemie International Edition* **49**, 6361 (2010).
- [32] Z. Swiatkowska-Warkocka, A. Pyatenko, F. Krok, B. R. Jany, and M. Marszalek, *Scientific Reports* **5**, 9849 (2015).
- [33] P. R. Subramanian and J. H. Perepezko, *Journal of Phase Equilibria* **14**, 62 (1993).
- [34] Y. Lei, F. Chen, Y. Jin, and Z. Liu, *Nanoscale Research Letters* **10** (2015), 10.1186/s11671-015-0900-9.
- [35] P. P. Kiran, B. N. Shivakiran Bhaktha, D. N. Rao, and G. De, *Journal of Applied Physics* **96**, 6717 (2004).
- [36] L.-u. Rahman, A. Shah, S. K. Lunsford, C. Han, M. N. Nadagouda, E. Sahle-Demessie, R. Qureshi, M. S. Khan, H.-B. Kraatz, and D. D. Dionysiou, *RSC Advances* **5**, 44427 (2015).

- [37] S. Das, R. N. P. Vemuri, and T. L. Alford, *Journal of Vacuum Science & Technology B* **31**, 011204 (2012).
- [38] O. Oudbashi and A. Shekofteh, *PERIODICO di MINERALOGIA* **84** (2015), 10.2451/2015PM0022.
- [39] D. Ashkenazi, H. Gitler, A. Stern, and O. Tal, *Scientific Reports* **7**, 40659 (2017).
- [40] P. A. Dmitriev, S. V. Makarov, V. A. Milichko, I. S. Mukhin, A. S. Gudovskikh, A. A. Sitnikova, A. K. Samusev, A. E. Krasnok, and P. A. Belov, *Nanoscale* **8**, 5043 (2016).
- [41] H. Kabbara, J. Ghanbaja, C. Nol, and T. Belmonte, *Materials Chemistry and Physics* **217**, 371 (2018).
- [42] T. Belmonte, C. Nol, T. Gries, J. Martin, and G. Henrion, *Plasma Sources Science and Technology* **24**, 064003 (2015).
- [43] P. J. Bruggeman, N. Sadeghi, D. C. Schram, and V. Linss, *Plasma Sources Science and Technology* **23**, 023001 (2014).
- [44] Y. Zhang, J. R. G. Evans, and S. Yang, *Journal of Chemical & Engineering Data* **56**, 328 (2011).
- [45] A. Hamdan, C. Noel, F. Kosior, G. Henrion, and T. Belmonte, *The Journal of the Acoustical Society of America* **134**, 991 (2013).
- [46] A. Pyatenko, H. Wang, N. Koshizaki, and T. Tsuji, *Laser & Photonics Reviews* **7**, 596 (2013).
- [47] N. Tarasenko, V. Kiris, E. Stankevicius, N. Tarasenko, V. Pankov, F. Krma, P. Geys, and G. Raiukaitis, *ChemPhysChem* **19**, 3247 (2018).
- [48] N. A. Kirichenko, I. A. Sukhov, G. A. Shafeev, and M. E. Shcherbina, *Quantum Electronics* **42**, 175 (2012).
- [49] V. K. Pustovalov, *Chemical Physics* **308**, 103 (2005).
- [50] P. Buffat and J.-P. Borel, *Physical Review A* **13**, 2287 (1976).
- [51] G. P. Zograf, M. I. Petrov, D. A. Zuev, P. A. Dmitriev, V. A. Milichko, S. V. Makarov, and P. A. Belov, *Nano Letters* **17**, 2945 (2017).
- [52] P. B. Johnson and R. W. Christy, *Physical Review B* **6**, 4370 (1972).
- [53] J. Song, H. Li, J. Li, S. Wang, and S. Zhou, *Applied Optics* **41**, 5413 (2002).